

REVIEW

Open Access



Perspectives on interfacial thermal resistance of 2D materials: Raman characterization and underlying physics

Jing Liu^{1†}, Ibrahim Al Keyyam^{2†}, Yangsu Xie^{3*} and Xinwei Wang^{2*}

Abstract

Interfacial thermal resistance plays a crucial role in efficient heat dissipation in modern electronic devices. It is critical to understand the interfacial thermal transport from both experiments and underlying physics. This review is focused on the transient opto-thermal Raman-based techniques for measuring the interfacial thermal resistance between 2D materials and substrate. This transient idea eliminates the use of laser absorption and absolute temperature rise data, therefore provides some of the highest level measurement accuracy and physics understanding. Physical concepts and perspectives are given for the time-domain differential Raman (TD-Raman), frequency-resolved Raman (FR-Raman), energy transport state-resolved Raman (ET-Raman), frequency domain ET-Raman (FET-Raman), as well as laser flash Raman and dual-wavelength laser flash Raman techniques. The thermal nonequilibrium between optical and acoustic phonons, as well as hot carrier diffusion must be considered for extremely small domain characterization of interfacial thermal resistance. To have a better understanding of phonon transport across material interfaces, we introduce a new concept termed effective interface energy transmission velocity. It is very striking that many reported interfaces have an almost constant energy transmission velocity over a wide temperature range. This physics consideration is inspired by the thermal reffusivity theory, which is effective for analyzing structure-phonon scattering. We expect the effective interface energy transmission velocity to give an intrinsic picture of the transmission of energy carriers, unaltered by the influence of their capacity to carry heat.

Keywords Interfacial thermal resistance, 2D materials, TD-Raman, FR-Raman, ET-Raman, FET-Raman, Effective interface energy transmission velocity, Thermal reffusivity

1 Introduction

Since the emergence of two-dimensional (2D) materials, enormous interests have been attracted by their exceptional optical, thermal, and electric properties. One of the promising applications of 2D materials lies in nanoscale electronic devices such as field effect transistors. As 2D materials are integrated in electronic devices [1, 2], the substrate affects the phonon scattering in 2D materials so their thermal transport properties change dramatically from those of suspended ones [3]. The heat dissipation and thermal performance of 2D material devices are tightly related to their interfacial thermal conductance/resistance [4, 5]. Thus, it is critical to understand the

[†]Jing Liu and Ibrahim Al Keyyam equally contributed to this work.

*Correspondence:

Yangsu Xie

ysxie@szu.edu.cn

Xinwei Wang

xwang3@iastate.edu

¹ College of New Materials and New Energies, Shenzhen Technology University, Shenzhen, Guangdong 518116, P. R. China

² Department of Mechanical Engineering, Iowa State University, Ames, IA 50011, USA

³ College of Chemistry and Environmental Engineering, Shenzhen University, Shenzhen, Guangdong 518055, P. R. China

interfacial thermal transport both from physical perspectives and experiments.

Experimental work and molecular dynamics simulations have been done for better understanding the atomic-scale thermal contact resistance of low-dimensional materials as summarized in our previous work [6]. For interfacial thermal resistance/conductance measurements, a methodology is to create a heat flux across the interface and detect the temperature difference between the 2D material and substrate. Based on heating and temperature sensing methods, the techniques can be classified into two categories: electrical-heating and laser heating techniques. The 3ω technique belongs to the electrical heating category [7]. The laser heating method includes photothermal radiation technique (PTR) [8–10], time-domain thermo-reflectance (TDTR) [11–15], frequency-domain thermo-reflectance (FDTR) [16–18], and steady state Raman (SS-Raman) techniques [19–23]. The 3ω method is a contact technique that employs electrical heating and temperature sensing based on electrical resistance-temperature relationship. A metallic film deposited on the sample serves as both heater and temperature sensor. During experiment, an alternating current (AC) with ω frequency is fed to the sample, which leads to temperature and electrical resistance change at 2ω frequency. Finally, the voltage change at 3ω frequency is detected by a lock-in amplifier. The interfacial thermal resistance can be extracted from the measured temperature response under different frequencies [7]. The PTR technique employs an amplitude-modulated laser (50% duty) to heat the sample surface. The thermal radiation from the surface is then detected by an infrared detector with a lock-in amplifier, which outputs information on the amplitude and phase shift (time delay) between temperature rise and incident laser. Based on this, the interfacial thermal resistance can be extracted [9].

The TDTR technique detects the optical reflectivity change due to temperature change to obtain the thermal responses of sample after ultrafast pulsed laser heating [24]. A femo/picosecond laser pulse is split into two beams. One serves as the pump beam to heat the sample while another beam acts as the probe beam to detect the thermoreflectance (Z) whose intensity change is proportional to the surface temperature rise. The time delay between the pump and probe beams is controlled by varying their optical path. By detecting the temporal decay of sample surface during cooling period, the interfacial thermal conductance can be extracted [13, 15]. It has been successfully applied in measuring the interface thermal conductance of $\text{Ga}_2\text{O}_3/\text{diamond}$ [25], $\text{GaN}/\text{diamond}$ [26], $\text{graphene}/\text{GaN}$, and MoS_2/GaN [27]. In this technique, the modulation frequency should be properly selected to ensure

high sensitivity of the detected signal to thermal properties. However, this sensitivity is closely related with unknown thermal properties, thus it is difficult to determine the modulation frequency before measurement. The FDTR technique is further developed to overcome this problem and reduce the complexity of mechanical delay. Instead of detecting the thermo-reflectance signal as a function of delay time, it detects the thermo-reflectance signal as a function of modulation frequency of the pump beam [16, 18]. By fitting the thermo-reflectance against the modulation frequency curve, thermal properties such as thermal conductivity and interfacial thermal resistance can be obtained.

Among the above reviewed techniques, the 3ω method employs electrical heating and has higher measurement accuracies than the laser-assisted techniques. However, the sample preparation is complex and time-consuming [28]. The PTR technique employs surface laser heating and thermal radiation measurement from the heated surface to extract the interfacial thermal resistance [8, 9]. Under cryogenic temperatures, the peak thermal radiation wavelength becomes very long (e.g. 0.145 mm at 20 K) which is difficult to detect. Thus, the PTR technique is difficult to use in cryogenic tests [24]. The advantages of TDTR and FDTR include simple sample preparation, versatile capability of determining multiple thermophysical properties and high temporal and spatial resolutions [24]. Though TDTR has been successfully applied in interface thermal conductance measurement between graphene and metal [29, 30], it has the following disadvantages in thermal property characterization of 2D materials. For optically transparent materials like 2D materials, the surface thermo-reflectance is affected by the temperatures of both 2D material and substrate, which cannot be differentiated in the signal. Besides, treatment by depositing a metallic film on the 2D material (making a sandwich structure) will significantly change the morphology of the 2D material, its interface structure, and the local thermal transport properties.

The above problem can be resolved by using Raman-based techniques. The characteristic peaks in Raman spectrum of 2D materials have strong temperature dependence, and can be used to probe and distinct its temperature from that of the substrate. Its non-contact and non-destructive feature makes the Raman technique a powerful tool for thermal characterization. A large number of materials have their unique Raman peaks. The Raman shift, linewidth, and intensity are temperature dependent, which can be used for efficiently monitoring the temperature of 2D materials. In addition, derivative parameters from the unique Raman signals, for example, the resonance Raman ratio (R3) of WS_2 has been proven to be a robust and high-sensitive

tool for temperature probing in the temperature range of from 170 to 470 K [31].

The first developed Raman-based thermal characterization technique is steady-state Raman (SS-Raman). The SS-Raman employs one single continuous wave (CW) laser beam to heat the sample and excite Raman signals at the same time. The Raman shift temperature coefficient (χ_T) and Raman shift as a function of absorbed laser power (P) is obtained. Based on the determined temperature rise under a specific laser power, the interfacial thermal resistance can be determined [23]. However, the laser absorbance evaluation and temperature calibration may introduce very large uncertainties in interfacial thermal resistance determination. The laser absorbance is determined by the optical properties of 2D material and substrate. For a supported 2D material, the local optical interference leads to low accuracy in the laser absorbance calculation. The temperature rise of 2D material requires Raman shift temperature coefficient ($\chi_T = \partial\omega/\partial T$) calibration in a separate experiment. During temperature calibration, the 2D material is in thermal equilibrium with the substrate. However, it experiences a very large lateral temperature gradient and large temperature difference across the interface under the laser heating during interface characterization. The resulting strain in the 2D material affects the Raman shift, which will introduce errors in temperature rise analysis and laser absorption evaluation if interface delamination happens [32, 33]. The mechanism of Raman spectrum response to temperature and possible error factors in calibration and measurement, as well as physical problems faced in Raman-based thermal characterization of 2D materials have been comprehensively discussed in our previous work [33, 34].

In recent years, Raman based thermal characterization techniques have been developed from SS-Raman to transient opto-thermal Raman, which provide more powerful tools for extreme thermal probing and pave the way for studying novel physical phenomena in interfacial energy transport. In this paper, we systematically review the transient opto-thermal Raman-based techniques for measuring the interfacial thermal resistance between 2D materials and substrate. Compared with the SS-Raman, transient Raman techniques avoid the large uncertainties from laser absorption coefficient and absolute temperature rise estimation. We discuss the physical principles, critical features, advantages, and applications of each unique technique. In addition, to have a better understanding of phonon transport across the 2D material interface, we introduce a new concept termed effective interface energy transmission velocity and discuss its effect on interface thermal conductance. The goal of

this perspective is to provide critical guidance for understanding the interfacial thermal transport from both the Raman measurement techniques and underlying physics.

2 Transient Raman techniques for 2D material interface characterization

Based on aforementioned limitations of SS-Raman, researchers are seeking Raman-based techniques without needing the laser absorption coefficient and absolute temperature rise. A good physical methodology proposed by Wang's group is to create different transient energy transport states to rule out the need of absolute temperature rise and laser absorption coefficient [35–37]. In this section, we will discuss the physical principles of transient thermal response in time domain of time-domain differential Raman (TD-Raman) [37], in frequency domain of frequency-resolved Raman (FR-Raman) [36], accumulated response during an extremely short time of frequency domain energy transport state-resolved Raman (FET-Raman) [35, 38] and energy transport state-resolved Raman (ET-Raman) [39, 40]. Zhang's lab also developed two promising Raman techniques based on transient thermal response to determine the thermophysical properties of micro/nanoscale materials: laser flash Raman [41, 42] and dual-wavelength laser flash Raman [43, 44].

2.1 Hot carrier diffusion and nonequilibrium phonons in 2D materials under laser irradiation

Before discussing the transient Raman techniques to characterize the thermophysical properties of 2D materials, it is critical to understand the energy transfer among carriers in a 2D material during and after laser irradiation. The carriers include photons, electrons, optical phonons (OPs) and acoustic phonons (APs). Figure 1 shows the physics of hot carrier generation, diffusion and recombination in MoS₂ under a CW 532 nm (2.33 eV) laser irradiation [40]. Upon laser irradiation, the electrons in valence band are excited to conduction band by absorbing photons, leaving holes in the valence band. In an extremely short time (0.5~1 ps), the excited electrons lose excess energy ($\Delta E = E_v - E_g$, E_v : photon energy, E_g : bandgap) by exciting phonons through a fast thermalization process. The electrons carrying the remained photon energy will diffuse out of the excitation area (related to the laser spot radius) [45, 46]. Then the excited electrons and holes recombine through a non-radiative process to release energy for multilayered 2D materials, and through a radiative process for monolayers. In both thermalization and recombination processes, the energy is transferred from hot electrons to lattice (phonons). Theoretical research has shown that the hot electrons relax mainly through optical phonons emission [47]. Due to

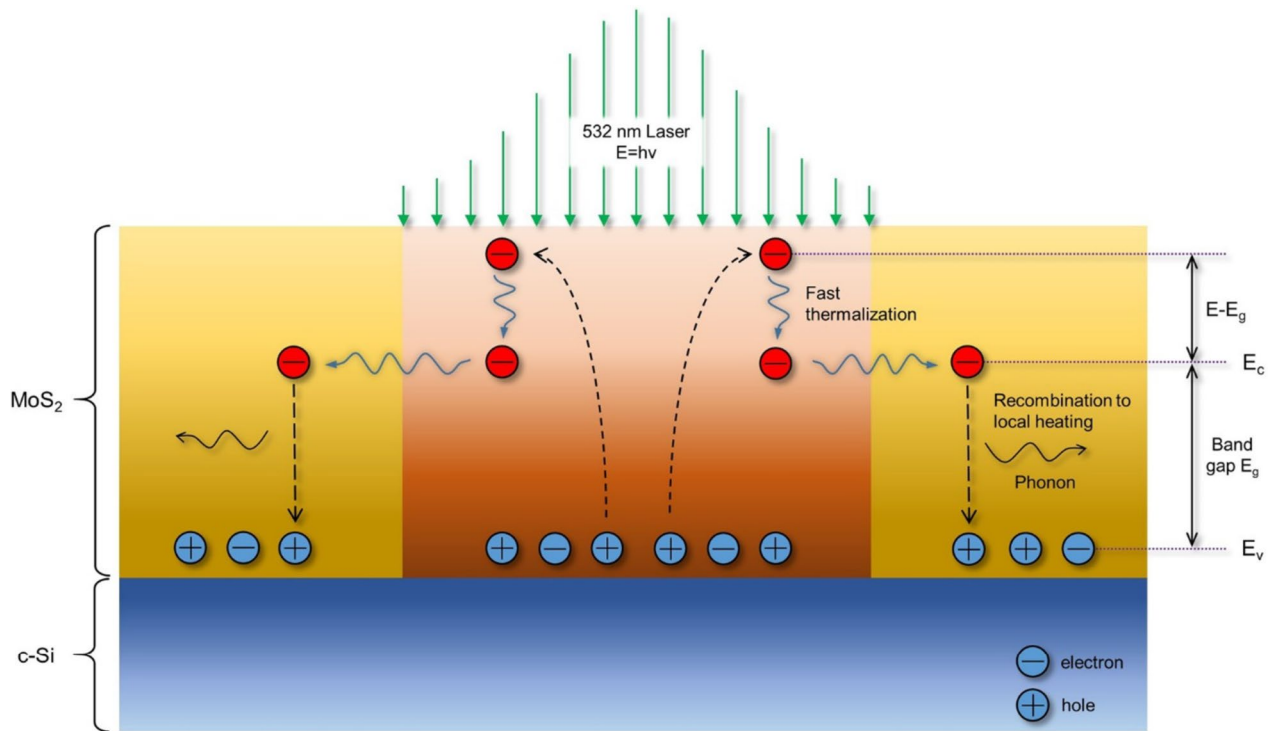


Fig. 1 Schematic of hot carriers' generation, diffusion and recombination in MoS₂ under 532 nm CW laser irradiation [40]. (Not to scale) (Reprinted from Ref. [40]. Reproduced with permission of Royal Society of Chemistry. All rights reserved)

the low group velocity of OPs, most of the energy carried by OPs will transfer to APs which sustain the majority of heat conduction [47].

The governing equation of hot carriers energy transfer can be expressed as [45]:

$$D\nabla^2\Delta N - \frac{\Delta N}{\tau} + \frac{\partial n_0}{\partial T} \frac{\Delta T}{\tau} + \Phi\alpha = 0 \quad (1)$$

Here, D , τ and Φ are the carrier diffusion coefficient, electron-hole recombination time and the incident photon flux. α (cm⁻¹) is the optical absorption coefficient of 2D materials. n_0 (cm⁻³) is the equilibrium free-carrier density at temperature T . The second governing equation (energy transport) involves the electron-hole recombination process and energy transfer among lattice (phonons) [45]:

$$\kappa\nabla^2\Delta T + (h\nu - E_g)\Phi\alpha + \frac{E_g}{\tau}(1 - \beta) = 0 \quad (2)$$

Here, $\Delta T(r, t)$ and κ are the temperature rise and thermal conductivity of a 2D material. $h\nu$ is the photon energy of the laser source. β is the electron-hole radiative recombination efficiency (for monolayer). In supported 2D materials, the heat will transfer from the lattice of 2D material to substrate, where the

interfacial thermal resistance dominates this process. The heat transfer across the interface can be described as $q'' = (T_{2D} - T_s)/R''_{tc}$, where q'' and R''_{tc} are the heat flux across the interface and the local interfacial thermal resistance.

Two critical points should be discussed here. Under laser irradiation, the excited electrons diffuse out of the laser spot area, which results in a heating area larger than the laser spot. It has been reported that the hot carrier diffusion length in few-layered MoS₂ is in the order of a few 0.1 μm , which is comparable to the laser heating spot size under 100 \times objective (0.3 μm radius) [36]. The underestimated heating area leads to an overestimated laser heating flux which finally lowers the determined interfacial thermal resistance. The hot carrier generation and diffusion have been extensively studied by the Schottky diode method [48–51]. However, the Schottky diode method can only investigate the hot electron diffusion in metal-2D material diode where the hot electron diffusion will be different from that in 2D material under laser irradiation. Thus, it is critical to take the hot carrier diffusion into account simultaneously when the thermal transport in 2D material is investigated. In addition, Ruan et al. reported that under laser irradiation, different phonon branches are in strong thermal nonequilibrium, with the ratio of temperature rise of phonon branches as high

as six [47]. A multitemperature model (MTM) was developed by using phonon branch-resolved e - p coupling factors to predict the phonon branch-resolved temperature under laser irradiation [52]. The results show that within the laser spot area, different phonon modes are in thermal nonequilibrium, especially flexural phonons showing the largest nonequilibrium from other phonon modes. The Raman-based technique has assumed that the phonons are in thermal equilibrium and the detected temperature by Raman shift is the lattice temperature. Since the determined interface thermal conductance is inversely proportional to the temperature difference between 2D material and substrate, it is critical to assess the interphonon thermal nonequilibrium when using Raman-based techniques. Based on the above analysis, taking the hot carrier diffusion and interphonon thermal nonequilibrium into consideration is essential in high-level characterization of 2D material interfacial thermal resistance.

2.2 Time-domain differential Raman (TD-Raman)

The time-domain differential Raman (TD-Raman) was the first Raman-based technique that detects the transient thermal response of samples for thermophysical characterization. The TD-Raman employs a square-wave amplitude modulated laser with varying duties to realize different heating state and transient thermal response probing. Figure 2 shows the physical concept of TD-Raman [37]. With the pulse-on period increasing from a short one to a sufficiently long one, the final state in the sample transits from transient state to steady state. The pulse-off period is fixed and long enough for the sample to cool down before the next pulse comes in, so there is no heat accumulation from the previous cycle [37].

The TD-Raman was validated by measuring a tipless Si AFM cantilever. A square-wave modulated laser irradiated the tip end. The heat conduction in the Si cantilever can be regarded as one-dimensional. Since the detected Raman signal reflects the temperature in the whole heating area and pulse-on period, the temperature rise was integrated in both whole heating time and heating area. The pulse-on period time was carefully designed from 20 μ s to 2 ms. By fitting the Raman shift or Raman peak intensity variation against laser pulse-on time, the thermal diffusivity of Si was determined successfully.

The TD-Raman fits the normalized Raman emission and Raman wavenumber change with the heating time, so no temperature calibration was needed. Also, since the irradiating laser intensity is the same in different heating period, the temperature difference (ΔT_{OA}) between OPs and APs is constant. Therefore, the Raman shifts caused by ΔT_{OA} are constant, which will not affect the fitting result. However, when the

laser pulse-on time is extremely short like 20 μ s (which is needed for characterizing very fast heat conduction processes), the Raman signal becomes very weak. The integration time in Raman spectroscopy could be as long as half an hour to get sound Raman spectra. This will introduce environmental interference to the experiment and downgrade the measurement accuracy.

2.3 Frequency-resolved Raman (FR-Raman)

To overcome the drawback of TD-Raman for very-short timescale thermal probing, the FR-Raman was developed for probing the transient thermal response. Figure 3 shows the physical concept of FR-Raman [53]. It employs a square-wave amplitude modulated laser with fixed 50% duty to heat the sample. Instead of varying the pulse-on period in TD-Raman, the FR-Raman varies the modulation frequency (f). The Raman signal is acquired during pulse-on period which reflects the time integral of temperature evolution during the heating period [36]. As shown in Fig. 3b and c, the temperature evolution is f -dependent. When f is very high, the temperature variations in both heating and cooling periods are very small and negligible. This state was named as 'quasi-steady state'. When f is very low, there is a sufficiently long time for the sample to reach steady-state during heating period and cool down to environmental temperature during cooling period. The FR-Raman was developed and validated by measuring a tipless Si cantilever. The Raman properties including Raman shift, Raman peak intensity, and linewidth vary with f , and can be used to determine the sample's thermal diffusivity.

The FR-Raman overcomes the drawback of TD-Raman for very-short timescale thermal probing and receives very good spectrum for data processing. At the same time, limited by the ability of modulator, the physical process shorter than nanoseconds is challenging to investigate. As the laser frequency is very high, there is no sufficient time for the sample to cool down to environmental temperature before next pulse. Under this situation, heat accumulation occurs, resulting in downgraded measurement sensitivity. The heat accumulation also requires many pulses calculation in numerical modelling, leading to extensive numerical calculation in data processing. The same as the TD-Raman, the FR-Raman eliminates the temperature calibration error in determining thermal properties since it only uses Raman properties $\sim f$ shape to determine thermal properties. Additionally, ΔT_{OA} is constant under different modulation frequencies, therefore the interphonon thermal nonequilibrium will not introduce errors into the thermal property determination.

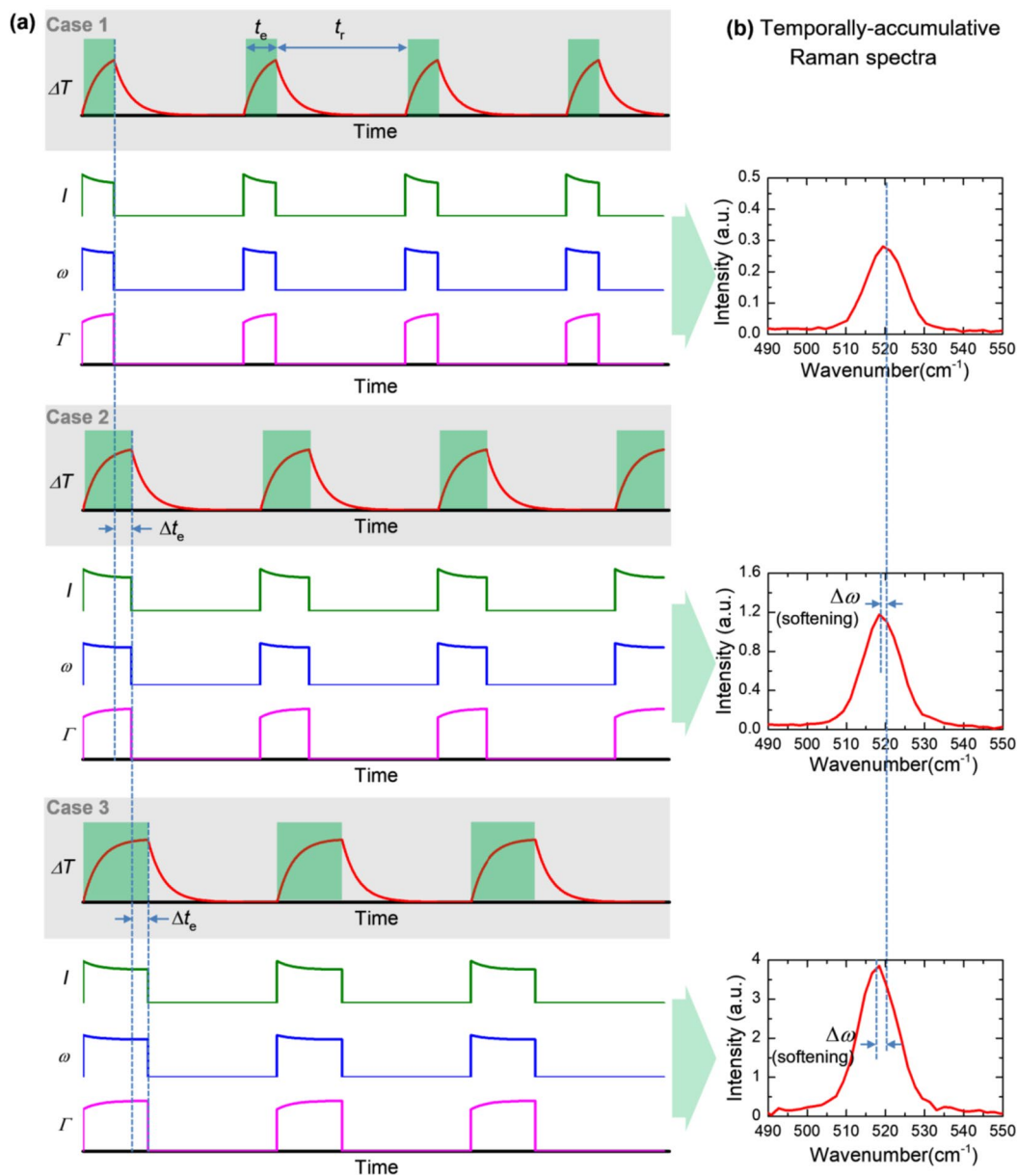


Fig. 2 Physical concept of the TD-Raman. **a** Evolution of temperature rise, Raman intensity (I), Raman shift (ω) and Raman peak linewidth (Γ) under different pulse-on periods. **b** Temporally-accumulative Raman spectra under different pulse-on periods [37]. (Reprinted from Ref. [37]. Reproduced with permission of Optical Society of America. All rights reserved)

2.4 Frequency-domain energy transport state resolved-Raman (FET-Raman)

Development of the FET-Raman is intended to eliminate the need of so many frequencies measurement in FR-Raman, and still achieve the same level accuracy, or even improve it. The FET-Raman employs a CW laser and an amplitude-modulated laser (frequency f) to heat the 2D material and create two distinct energy transport states. Figure 4 shows the detailed physical

concept of FET-Raman. In the case of steady-state heating by a CW laser, the substrate thermal resistance can be approximated as $R_{sub,CW} = \int_0^{\infty} (2\pi\kappa_{sub}r^2)^{-1} dr$, where κ_{sub} is the thermal conductivity of substrate. In the amplitude-modulated heating case, the thermal diffusion length into the substrate is much shorter, limited by the heating time, can be approximated as $L_T = \sqrt{\pi a_{\perp}/f}$, where a_{\perp} is the cross-plane thermal

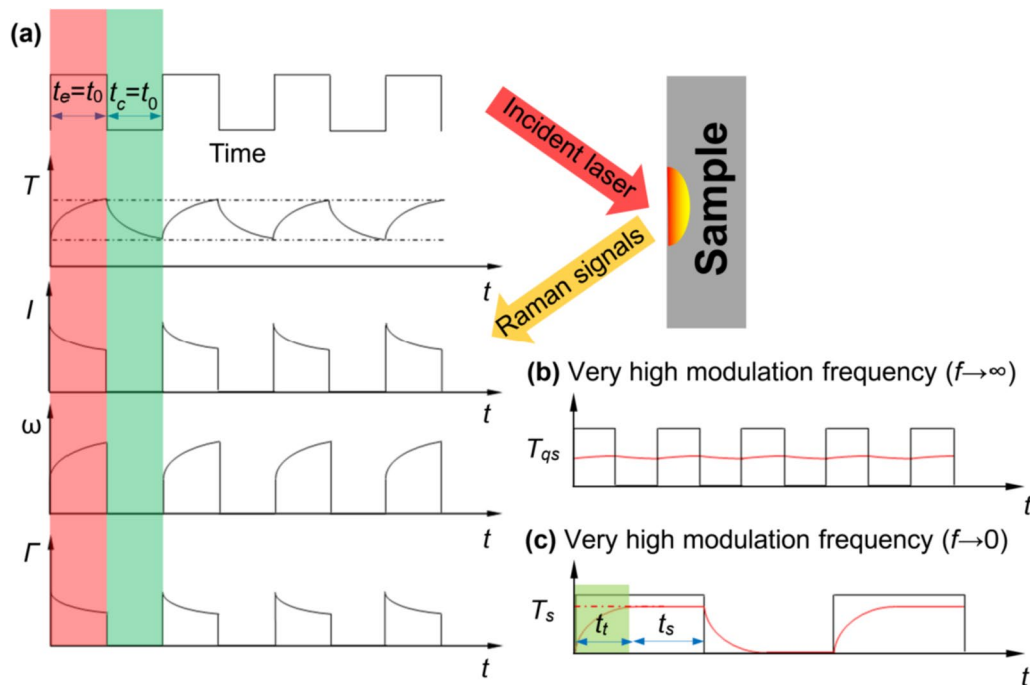


Fig. 3 Physical concept of the FR-Raman technique. **a** Pulsed laser heating, temperature evolution, Raman intensity, Raman shift and Raman peak intensity change with time. **b** The quasi-steady state and temperature evolution under very high f . **c** The steady state and temperature evolution under very low f . [53] (Reprinted from Ref. [53]. Reproduced with permission of Optical Society of America. All rights reserved)

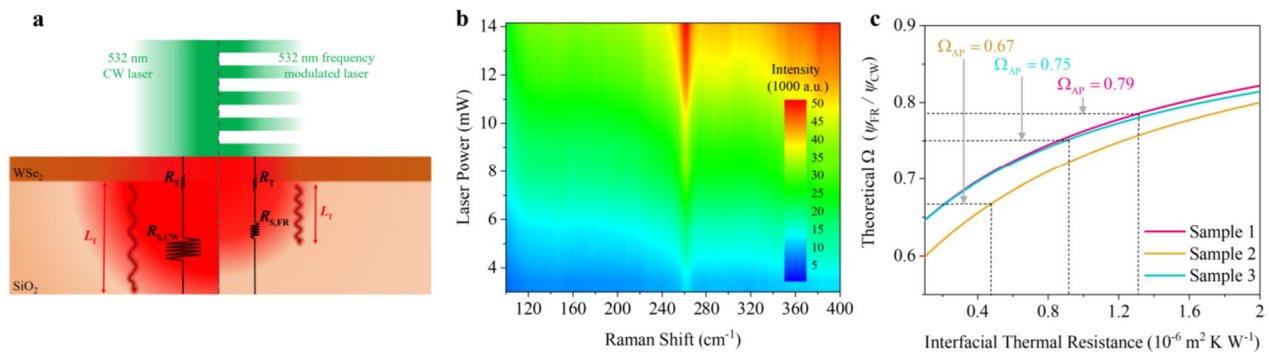


Fig. 4 **a** Physical concept of FET-Raman. **b** The 2D Raman intensity contour at different modulated laser powers to show the characteristic WSe_2 Raman signal near 260 cm^{-1} . **c** Determination of interfacial thermal resistance by the experiment-obtained Ω . [38] (Reprinted from Ref. [38]. Reproduced with permission of WILEY-VCH. All rights reserved)

diffusivity of the substrate and f is the modulation frequency. The resulting substrate thermal resistance is approximated as $R_{sub,FR} = \int_0^{L_T} (2\pi\kappa_{sub}r^2)^{-1} dr$. The total thermal resistance (R_{total}) is the summation of interfacial thermal resistance (R_T) and substrate thermal resistance (R_{sub}): $R_{total} = R_T + R_{sub}$. The contribution of R_T to R_{total} is much stronger under amplitude-modulated laser heating. Therefore, the interfacial thermal resistance can be obtained by investigating the thermal response in these two distinct energy transport states.

As a CW laser irradiates a supported 2D material with different laser power (P), the Raman shift (ω) power coefficient (RSC) of the steady state case (ψ_{CW}) is $\psi_{CW} = \partial\omega/\partial P$. ψ_{CW} depends on laser absorption coefficient (α), Raman shift temperature coefficient ($\partial\omega/\partial T$), the thermal conductivity (κ_{2D}) of 2D material and substrate (κ_{sub}), and interfacial thermal resistance (R''_{tc}) as: $\psi_{CW} = \alpha \cdot \partial\omega/\partial T \cdot f_{CW}(\kappa_{2D}, \kappa_{sub}, R''_{tc}, \rho c_p)$. By choosing an appropriate frequency (f) and collecting the Raman signals under different laser powers, the RSC in frequency-resolved Raman state can be obtained:

$\psi_{FR} = \alpha \cdot \partial\omega/\partial T \cdot f_{FR}(\kappa_{2D}, \kappa_{sub}, R''_{tc}, \rho c_p)$. To rule out the effect of laser absorption and Raman shift temperature coefficient, a normalized RSC (Θ) is used and defined as $\Theta = \psi_{FR}/\psi_{CW}$. It is clear that Θ is a function of R''_{tc} as the thermal conductivity of 2D material and substrate and volumetric heat capacity are known. Numerical modeling can be used to evaluate Θ and determine R''_{tc} . Note in all Raman-based measurements, the measured thermal response in fact is a Raman intensity weighted average in spatial and time domains. Such fact should be considered rigorously in data processing.

Since the FET-Raman probes the transient thermal response in the heating period, there is a temperature difference between OPs and APs in the 2D material. Wang et al. further developed a method which will be discussed later to determine the intrinsic thermal conductivity and interfacial thermal resistance with consideration of OP-AP thermal nonequilibrium [38, 54–57]. In FET-Raman, the duty is 50%, so the Raman signal is strong enough for data processing. However, the sample cannot cool down completely as the laser-off period is equal to the laser-on period. The heat accumulation in the sample hinders the measurement sensitivity.

2.5 Laser flash Raman spectroscopy

The laser flash Raman spectroscopy was first developed by Zhang's group [58–61]. In this technique, a series of square laser pulses are used to heat the sample and realize simultaneous Raman excitation. Between two adjacent pulses, the interval time is long enough for the sample to cool down to prevent heat accumulation. The average temperature rise of the 2D material and substrate

can be simultaneously determined by Raman signals. The laser flash Raman spectroscopy shares the similar principle with the TD-Raman. By varying the laser pulse duration (t_h) and laser spot radius, the average temperature rise will change, which can be used to determine thermal properties. By fitting the normalized T - t_h curve, the interfacial thermal resistance and thermal conductivity of a 2D material can be determined [59].

2.6 Dual-wavelength laser flash Raman spectroscopy

The temporal resolution of the laser flash Raman is limited by the rising time of the electro-optical modulator (EOM) signal. To push the temporal resolution of Raman spectroscopy to hundreds of picoseconds, Fan et al. developed a transient method called “dual-wavelength laser flash Raman spectroscopy” with the temporal resolution being pushed down to 100 ps [43, 59]. As shown in Fig. 5, a square wave-modulated laser is used to heat the sample. The temperature variation during the heating and cooling period is detected by a delayed pulsed laser with different wavelength and negligible heating effect. To eliminate the Raman shift peaks excited by the heating pulse, an appropriate cut-off filter or changing the grating position of the Raman spectrometer is settled. By changing the delay time (t_d) between the probe and heating pulse, the temperature rise evolution during heating period and temperature fall evolution during cooling period can be obtained. This concept is similar to the transient thermal reflectance detection in TDTR. To eliminate the laser absorption coefficient in data processing, a normalized temperature rise to the highest measured one is used to determine the thermal diffusivity of

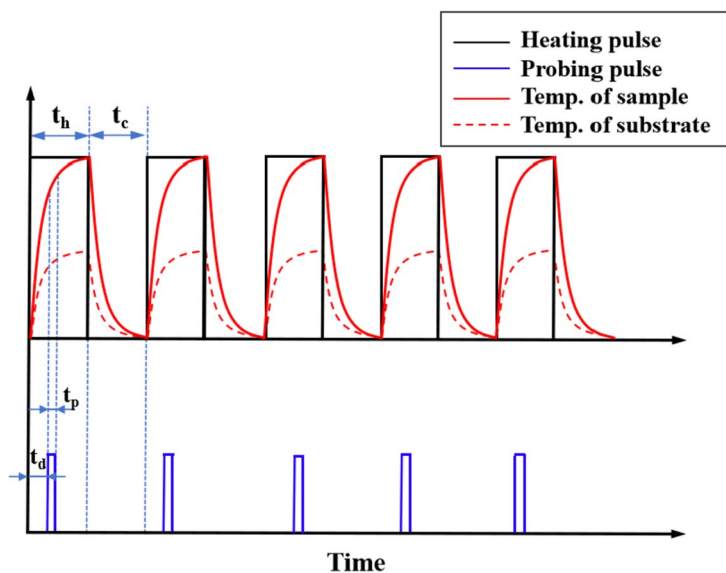


Fig. 5 Physical principle of the dual-wavelength laser flash Raman spectroscopy method

suspended materials. For supported materials, the temperature variation during the cooling period is obtained since it is not influenced by the laser absorption. In supported materials, the temperature variation of the substrate is affected by the interfacial thermal resistance. The normalized temperature rise of the 2D material carries the effect of the interfacial thermal resistance, and can be used to determine it.

When the temperature variation during the cooling period is used to determine the interfacial thermal resistance, the hot carrier diffusion has no effect since there is no hot carrier generation and heating. Also in the laser-off period, OPs and APs are in thermal equilibrium, so the measured temperature response reflects the true AP temperature. Similar to the TDTR technique, the complexity of experimental setup could hinder the wide application of dual-wavelength laser flash Raman spectroscopy.

2.7 Energy transport state-resolved Raman (ET-Raman): down to ps resolution and probing of hot carrier diffusion

In the abovementioned Raman-characterized physical processes, hot carriers diffuse out of the irradiated area until they recombine with holes, leading to an enlarged

heating area. This heating area is strongly interrelated with the hot carrier diffusion length [45], which could be comparable to the laser spot size. Recently, Wang's lab has done pioneering work about simultaneous determination of hot carrier diffusion coefficient (D) and interfacial thermal resistance (R) [39, 40, 45, 46, 62]. They developed a picosecond (ps) energy transport state-resolved Raman (ET-Raman) which realized a ps heat transfer scenario to directly probe the diffusion of hot carriers and their contribution to energy transfer. Figure 6 shows the schematic of ET-Raman for simultaneous measurement of D and R . As shown in Fig. 6c and d, the steady-state heating is accomplished by applying a CW (532 nm) laser. Under CW laser irradiation, different objective lenses (20 \times and 100 \times) were employed to differentiate the effect of D and R . By applying a picosecond laser (532 nm, the pulse duration is 13 ps, the repetition rate is 48.2 MHz), a near zero-transport state is constructed. Within such a short laser pulse (13 ps), no electron-hole recombination occurs. The temperature rise under ps laser heating is more determined by volumetric heat capacity (ρc_p), rather than the R and D .

To rule out the effect of laser absorption coefficient and Raman temperature coefficient, a normalized RSC

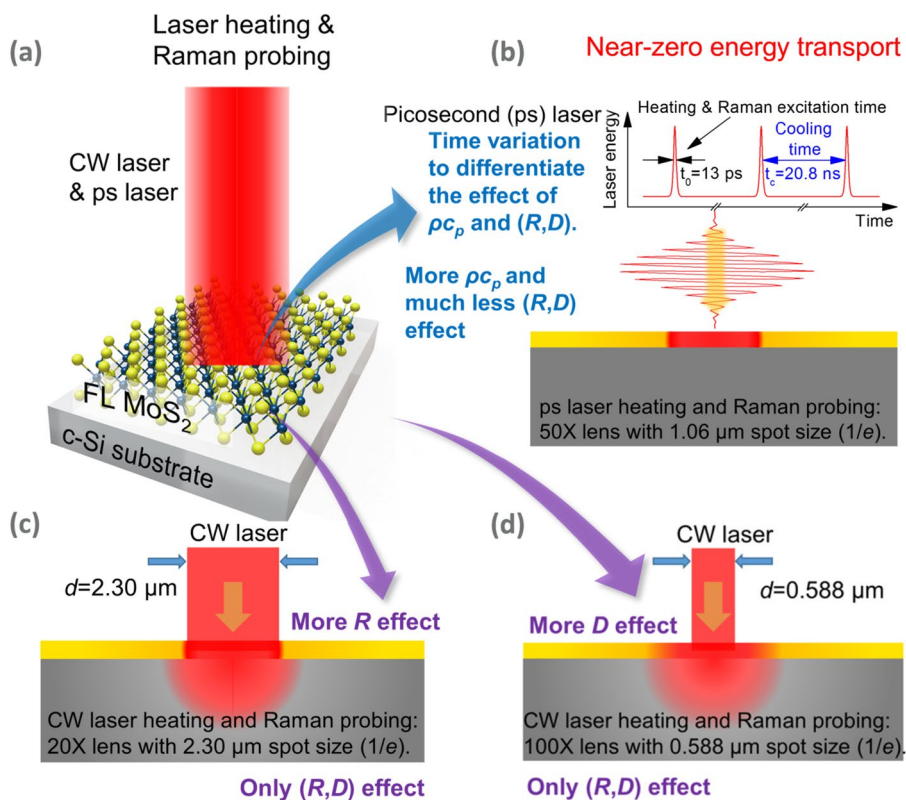


Fig. 6 a Schematic of CW and ps laser irradiating of MoS₂ on a Si substrate with simultaneous Raman probing. b-d Artistic representation of the ET-Raman experiment concept [45]. (Reprinted from Ref. [45]. Reproduced with permission of American Chemical Society. All rights reserved)

is defined as $\Theta_1 = \psi_{CW1}/\psi_{ps}$ and $\Theta_2 = \psi_{CW2}/\psi_{ps}$. The subscripts 'CW' and 'ps' represent CW laser and pico-second laser heating cases. The subscripts '1' and '2' represent different objective lens (20× and 100×). Θ_1 and Θ_2 are functions of ρc_p , R and D . By solving the 3D heat conduction and hot carrier diffusion equations numerically, the D and R of a 2D material can be determined. Figure 7 shows the determination of D and R as well as temperature rise distribution in MoS₂ under different laser heating and objective lenses.

The ET-Raman creates different energy transport states to differentiate the hot carrier diffusion and the interface thermal transport. The distinct energy transport states can be realized in temporal or space domains. It is worth noting that the hot carrier diffusion effect is important in supported 2D material, while in suspended 2D material, its effect on thermal transport is negligible since most of heat is conducted in the in-plane direction. While in supported 2D materials, the majority of heat flux is transferred from the

2D material to substrate. Under this situation, the hot carrier diffusion affects a lot in the temperature rise distribution. It has been proven that the temperature rise in a 2D material is more sensitive to D under smaller laser spot sizes. Thus, as the laser spot size is much larger than the hot carrier diffusion length, its effect on thermal property measurement can be neglected [40, 45, 46, 63].

In ET-Raman, when the interval time between two adjacent pulses is long enough for the sample to completely cool down, no heat accumulation occurs. The measurement sensitivity of the ET-Raman is high. However, since proportion of the pulse duration is very small (e.g. 0.06%) in one cycle, the Raman signal of a thin 2D material can be very weak. To assure sound Raman signal for data processing, the laser power to irradiate the thin 2D material can be very high, leading to damage or laser absorption saturation in 2D materials. The FET-Raman has advantages in resolving this issue, although its measurement sensitivity is lower than the ET-Raman.

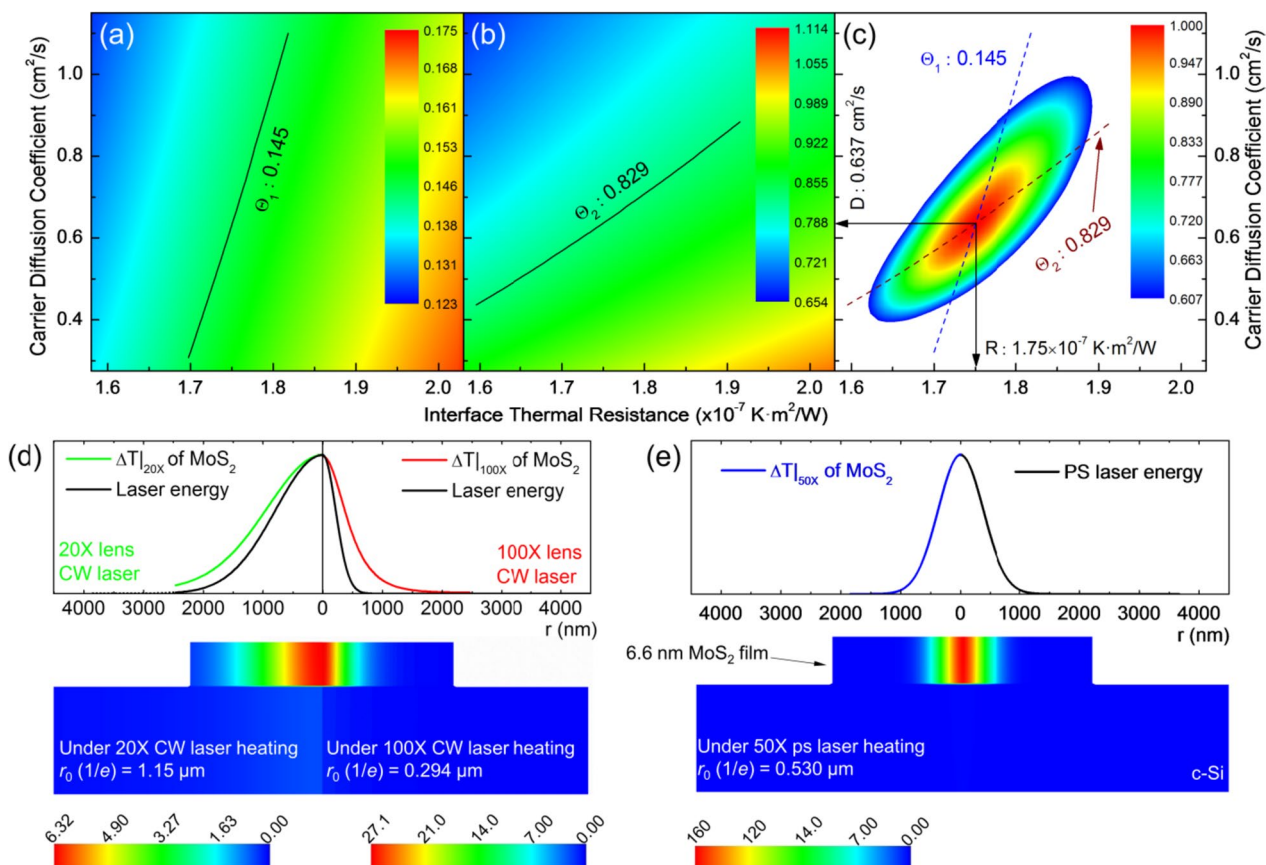


Fig. 7 a-c 3D numerical modeling results for determining D and R . d-e Temperature rise distribution in MoS₂ under CW laser heating with 20× and 100× objectives and ps laser heating under 50× objective [45]. (Reprinted from Ref. [45]. Reproduced with permission of American Chemical Society. All rights reserved)

2.8 Resolving thermal nonequilibrium among phonon branches

Regardless of different measurement principles in Raman techniques, under laser irradiation, the energy transfer in 2D materials all involves photon absorption, electron excitation and diffusion, electron–hole recombination and lattice heat conduction. The question to the reliability of Raman thermometry was first raised by Ruan’s lab [47, 52, 64]. They discovered that under laser irradiation, electrons, OP and AP are in strong nonequilibrium, especially for the flexural acoustic phonons which are the major heat carriers, showing the largest nonequilibrium from other phonon modes. However, the temperature rise detected by Raman thermometry reflects the temperature of OPs. Neglect of the nonequilibrium between OPs and APs will significantly limit the accuracy of thermal property

measurement from physics base and hinder the deep understanding of energy transport.

This OP and AP temperature distinguishing is very challenging and is achieved by using different behaviors of T_{AP} and T_{OP} in space and temporal domains. In the first work published in 2020, Wang’s lab first differentiated the temperature rise of OPs and APs by evaluating laser-spot-size dependent temperature rises [54]. Figure 8 shows the physics of thermal nonequilibrium between OPs and APs under laser irradiation [54]. The fundamental physics used in the work is: ΔT_{OA} is proportional to r_0^{-2} (r_0 : laser spot radius). Due to strong heat conduction by APs, the temperature rise of AP (ΔT_{AP}) has a weaker dependence on r_0 , namely $\Delta T_{AP} \propto f(\kappa) \cdot r_0^{-n}$ with $n < 2$. They firmly proved this physics base by first-principle calculation of graphene paper [54]. The temperature rise (ΔT_m) detected by Raman scattering is the temperature rise of OPs,

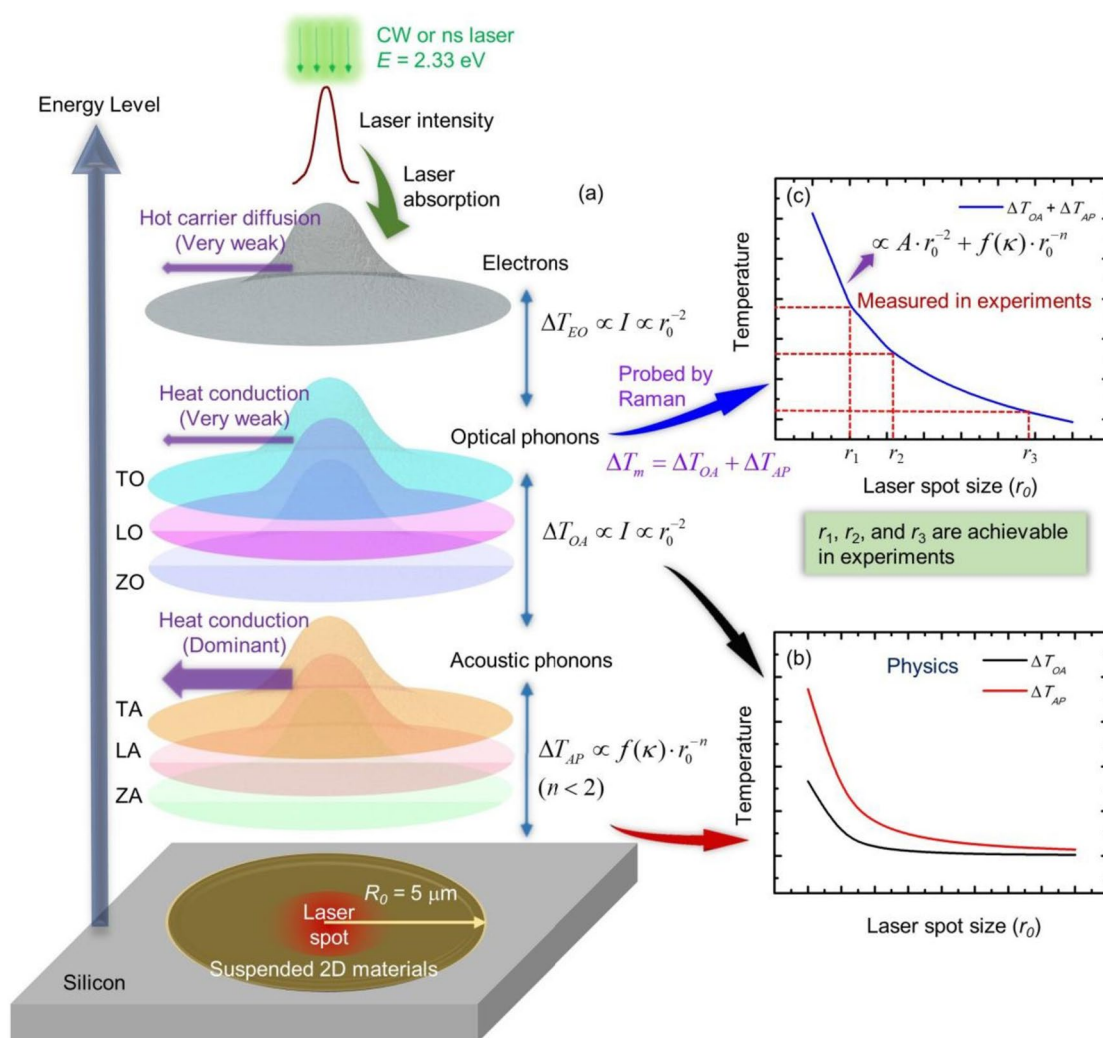


Fig. 8 Physics of thermal nonequilibrium between OPs and APs under laser irradiation [54]. (Reprinted from Ref. [54]. Reproduced with permission of WILEY-VCH. All rights reserved)

$\Delta T_m = \Delta T_{OA} + \Delta T_{AP} \propto Ar_0^{-2} + f(\kappa) \cdot r_0^{-n}$, as shown in Fig. 8c. ΔT_m is measured with different laser spot sizes. The obtained $\Delta T_m \sim r_0$ relationship is fitted with the function $Ar_0^{-2} + f(\kappa) \cdot r_0^{-n}$ to determine the contribution of ΔT_{OA} to ΔT_m .

The laser spot size in the above work [54] was limited by the experimental setup, which results in large fitting errors. Besides, this work needs intrinsic thermal conductivity while the intrinsic thermal conductivity was measured by neglecting this nonequilibrium. More importantly, the phonon mode nonequilibrium under CW and ns laser heating can be different due to different hot carrier densities. Xu et al. further developed this methodology by creating an AP thermal field invariant to rigorously distinguish the temperatures of OPs and APs without the need of intrinsic thermal conductivity of 2D materials [57]. In the experiment, a suspended WS_2 was used as an example for the study. The AP temperature rise ratio ξ_{AP} is defined as:

$$\xi_{AP} = \frac{\Delta T_{AP,1}}{\Delta T_{AP,2}} = \frac{\ln(r_h) - \ln(r_{i1})}{\ln(r_h) - \ln(r_{i2})} \quad (3)$$

where r_{i1} and r_{i2} are laser spot radius under different objectives. r_h is the radius of the hole for suspending

WS_2 . ξ_{AP} is found to be an invariant with negligible effect from the sample's thermal conductivity. Figure 9 shows this invariant for two different diameter samples. More details about the simulation can be found in reference [57]. The Raman spectroscopy in fact measures the OP temperature rise ratio ξ_{OP} [57]:

$$\xi_{OP} = \frac{\Delta \bar{T}_{OP,100\times}}{\Delta \bar{T}_{OP,20\times}} = \frac{\chi_T \cdot (\partial\omega/\partial P)_{100\times}}{\chi_T \cdot (\partial\omega/\partial P)_{20\times}} = \frac{(\partial\omega/\partial P)_{100\times}}{(\partial\omega/\partial P)_{20\times}} \quad (4)$$

where χ_T is the Raman shift temperature coefficient ($\chi_T = \partial\omega/\partial T$). Under unit incident laser power, the average temperature rise ($\Delta \bar{T}_{OP}$) detected by Raman can be expressed as:

$$\Delta \bar{T}_{OP} = \Delta \bar{T}_{AP,ri} + \Delta \bar{T}_{OA,ri} = \Delta \bar{T} + C_{OA}/r_i^2 \quad (5)$$

where C_{OA} is a constant. The subscript 'i' indicates different objective scenarios. With ξ_{AP} obtained from simulation and measured ξ_{OP} from experiments, the ratio (η) of $\Delta \bar{T}_{OA}$ to $\Delta \bar{T}_{AP}$ can be obtained.

The above thermal field invariant method provides probably the best method for distinguishing the temperatures of OPs and APs for suspended 2D materials.

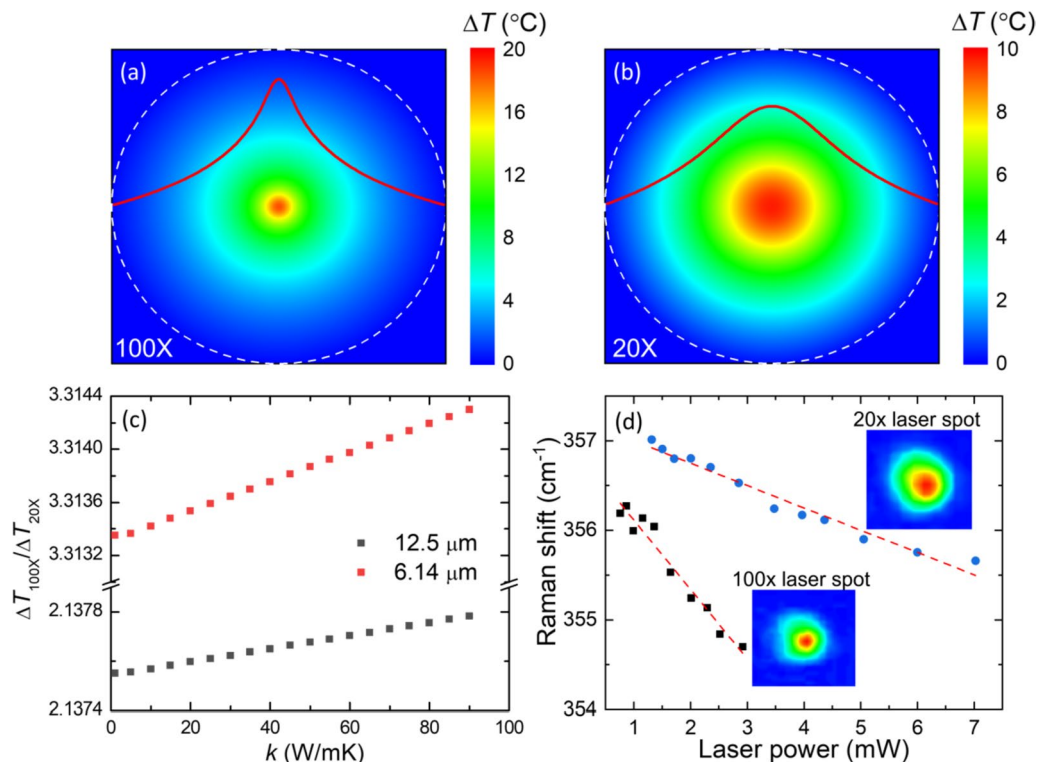


Fig. 9 a-b Temperature rise distribution in suspended WS_2 under 100 \times and 20 \times objective lens. c Simulated $\xi_{AP} = T_{AP,100\times}/T_{AP,20\times}$ variation against the intrinsic thermal conductivity for sample 1 suspended over a 12.5 μm hole and sample 2 suspended over a 6.14 μm hole. [57] (d) Raman shift laser power coefficient under 100 \times and 20 \times objective lens. (Reprinted from Ref. [57]. Reproduced with permission of Elsevier. All rights reserved)

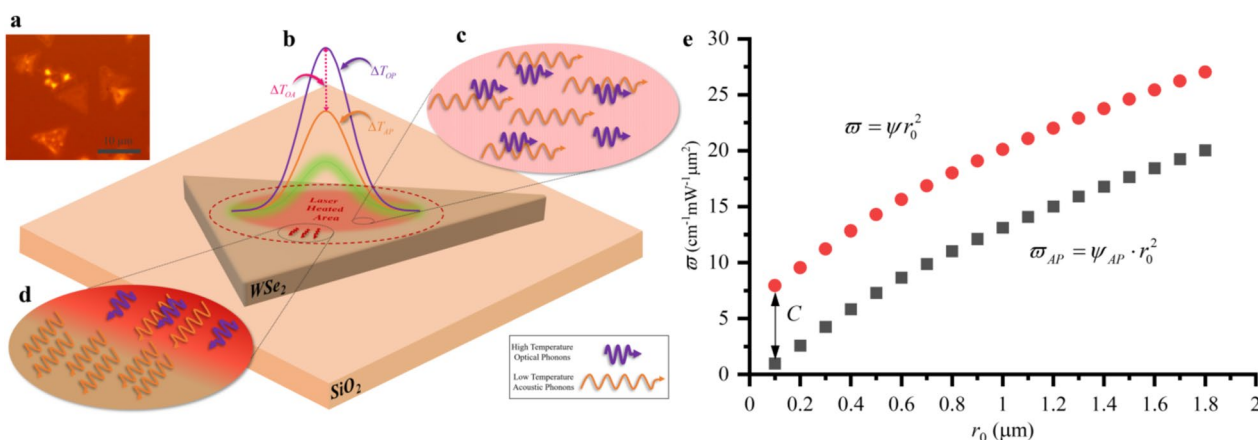


Fig. 10 Physics of thermal nonequilibrium between OPs and APs under laser irradiation. **a** Optical image of monolayer WS₂ on SiO₂. **b** Illustration of temperature rise under laser irradiation. **c** OPs (thicker wave packets) and APs (thinner wave packets) inside the laser heated area. **d** Only APs diffuse out of the laser spot at the edge of the laser heated area. **e** $\varpi \sim r_0^2$ relationship obtained by modeling a tri-layer MoS₂ on SiO₂ under 1 mW laser irradiation [38]. (Reprinted from Ref. [38]. Reproduced with permission of WILEY-VCH. All rights reserved)

This method is difficult to apply for supported 2D materials for interfacial thermal resistance characterization. Distinguishing OP and AP temperatures of supported 2D materials remains a big challenge, although some efforts have been tried. In the work published in 2021 [38], Wang's lab first differentiated the temperature rise of OPs and APs by evaluating laser spot size dependent Raman wavenumber coefficient ($\varpi = \psi r_0^2$, r_0 : laser spot radius) in a supported 2D material. Figure 10a shows the physics of thermal nonequilibrium between OPs and APs under laser irradiation in supported monolayer WS₂. The temperature rise of OPs (ΔT_{OP}) is the sum of temperature rise of substrate (ΔT_{sub}), temperature difference between the surface of the substrate and the supported 2D material (ΔT_{int}), and temperature difference between OPs and APs (ΔT_{OA}). The Raman shift power coefficient ψ is proportional to ΔT_{OP} which can be written as $\psi \propto \Delta T_{sub} + \Delta T_{int} + \Delta T_{OA}$. The key point to determine ΔT_{OA} is to find the laser spot size effect on the three temperature rise contributions listed above.

With analysis, ψ can be written as a function of the laser spot radius and arbitrary proportionality constants: $\psi = A/(r_0 + \Delta r) + B/(r_0 + \Delta r)^2 + C/r_0^2$. Here, a new parameter ϖ is defined as: $\varpi = \psi r_0^2$. This parameter represents the Raman wavenumber shift under unit laser peak intensity and termed as Raman shift intensity coefficient. ϖ can be expressed as $\varpi = Ar_0^2/(r_0 + \Delta r) + Br_0^2/(r_0 + \Delta r)^2 + C$. It is ready to find the contribution from ΔT_{OA} to ϖ is constant. Thus, the constant value C can be obtained by plotting the $\varpi \sim r_0$ relationship with r_0 approaches to zero as shown in Fig. 10e. With known C obtained from experiments, the temperature difference between OPs and APs can be

determined. More details about determining the temperature difference between OPs and APs in supported 2D materials and interface thermal conductance measurement can be found in the works of Wang's lab [38, 55].

3 Perspectives on ET-Raman

One critical feature of the ET-Raman is that the normalized RSC eliminates the need of temperature rise and laser absorption in interface thermal conductance (G) determination. Another critical feature and advantage of ET-Raman is that it significantly magnifies the effect of G of 2D materials on a substrate of low thermal conductivity (κ_s). In the measurement, under a laser spot of radius r_0 , under steady state laser heating the substrate's thermal resistance is $R_s = 1/(4r_0\kappa_s)$ and the interfacial thermal resistance is $R_i = 1/(\pi r_0^2 G)$. We have $R_i/R_s = 4\kappa_s/(\pi r_0 G)$. For a typical G of 10 MW·m²·K and r_0 of 2 μm, this ratio is 9.4 for a silicon substrate ($\kappa_s = 148$ W/m·K) and 0.09 for a fused silica ($\kappa_s = 1.4$ W/m·K). So for a 2D material on a fused silica, the temperature rise of the 2D material under steady state laser heating is largely determined by the thermal resistance of the substrate (>90%). The interfacial thermal resistance has negligible effect, making the measurement sensitivity very low for SS-Raman. In ET-Raman, the transient state heating using a pulsed laser in fact will strongly reduce the effect of substrate's thermal resistance, and significantly improve the measurement sensitivity. For instance, when the laser pulse width is 20 ns, the heat diffusion length (L_d) in fused silica during laser heating will be ~130 nm. The corresponding R_s of this thickness is about $L_d/(\pi r_0^2 \kappa_s)$. So we have $R_i/R_s = 1.08$, meaning the interfacial thermal resistance plays a big role in the probed thermal response of the 2D material.

In ET-Raman, the heating time design and selection is critical for high-sensitivity measurement. This transient energy transport state indeed is to reduce the effect of substrate and increase the effect of interfacial thermal resistance. This means the laser pulse width needs to be short enough so the substrate is far from reaching its steady state. The time (t_s) taken for the substrate to reach the steady state can be estimated as $t_s = (10r_0)^2/(\pi\alpha)$, here α is the thermal diffusivity of substrate. A characteristic thermal diffusion length of $10r_0$ is used here for the characteristic time estimation. Over this distance, the thermal resistance of the substrate is around $0.94/(4r_0\kappa_s)$, which is 94% of the steady state resistance. t_s is $\sim 1.4 \mu\text{s}$ for Si and 0.15 ms for fused silica with $r_0 = 2 \mu\text{m}$. This means the pulse width should be much shorter than this time so the effect of interfacial thermal resistance more stands out.

During pulsed laser heating, however, it takes a much shorter time for the 2D material to reach thermal equilibrium with the substrate surface. The corresponding characteristic time is $t_i = \Delta z \rho c_p / G$ with all the properties for the 2D material, Δz is the thickness of the 2D material. For a thickness of 10 nm and G of $10 \text{ MW}\cdot\text{m}^{-2}\cdot\text{K}$, t_i is 1.93 ns for MoS_2 . A monolayer 2D material usually has a thickness less than 1 nm, so t_i is around 0.2 ns or less. Therefore, during the pulsed laser measurement in ET-Raman, it is safe to assume that the 2D layer and the substrate reaches thermal equilibrium if a ns laser pulse is used.

4 Interfacial thermal conductance: effective interface energy transmission velocity

A. Background of the thermal reffusivity

In solid-state physics, the electron mobility (μ_e) characterizes how quickly an electron can move through a metal or semiconductor under an electric field. It is determined by the mean free time of electrons (τ_c) as $\mu_e = e\tau_c/m_e^*$, where m_e^* is the effective mass of an electron. Based on Matthiessen's rule, the scattering from multiple sources including the impurities and phonons can be combined to obtain the actual scattering effect: $\mu_e^{-1} = \mu_{\text{impurity}}^{-1} + \mu_{\text{phonon}}^{-1}$ as a good approximation. The electrical resistivity of metals is related to electron mobility and electron density (n) as: $\rho_e = 1/(en\mu_e)$. As a result, for metals, the electrical resistivity can be expressed as the sum of "residual electrical resistivity" caused by defect scattering and the temperature (T)-dependent resistivity which is resulted from phonon induced scattering. Such relation can be expressed based on the Bloch-Grüneisen formula as [65]:

$$\rho_e = \rho_0 + \alpha_p \left(\frac{T}{\theta}\right)^5 \int_0^{\theta/T} \frac{x^5}{(e^x - 1)(1 - e^{-x})} dx, \quad (6)$$

where θ is the Debye temperature. α_p is a constant, which is proportional to the electron-phonon coupling constant λ_{tr} . The "residual electrical resistivity" ρ_0 is induced solely by structural defects and often independent of temperature. Using the Fermi velocity, the mean free path resulted only from structure defects scattering, which reflects an effective structural domain size, can be evaluated from the ρ_0 value. Based on this model, the experimentally measured ρ_e - T curves of metals have historically been used for characterizing the structure and electrical resistivity relation. This also provides a powerful and convenient tool for studying structural defect levels, the Debye temperature, and the structural domain sizes in metals.

A general question is: Does thermal resistivity concept exist like electrical resistivity? Can it be used to characterize the structure characteristics and defect-induced energy carrier scattering? Unfortunately the inverse of thermal conductivity, although represents the thermal resistivity concept, cannot be used directly to explore the structure-scattering of energy carriers. In recent decades, theoretical studies of heat conduction in nanomaterials have developed complex phonon/electron models to have a better understanding of the relation between different structures and the corresponding thermal conductivity. For materials with phonons as the main heat carriers, based on the phonon dispersion relation, different phonon branches contribute to thermal conductivity based on their unique velocity, scattering, and phonon density of state [66–68]. Furthermore, four phonon scattering has been found to significantly reduce the intrinsic thermal conductivity of various solids [69, 70]. There are more complicated models that attempt to take other effects into account [66–68]. These advanced models significantly deepen our understanding of phonon propagation and thermal conductivity. Nevertheless, a simple yet very effective model is in demand for conveniently analyzing the experimental data and understanding the structure-thermal conductivity relationship.

From the single relaxation time approximation, for an isotropic material the thermal conductivity can be expressed as $\kappa = Cv l_s / 3$, where C is the energy carriers' heat capacity per unit volume, v is the average heat carrier velocity, and l_s is the mean free path of heat carriers. Based on this approximation, a new parameter named "thermal reffusivity (Θ)" has been proposed and the corresponding physical model has been developed by Wang's group in recent years to directly characterize the phonon and electron scattering [71–73]. For electrons,

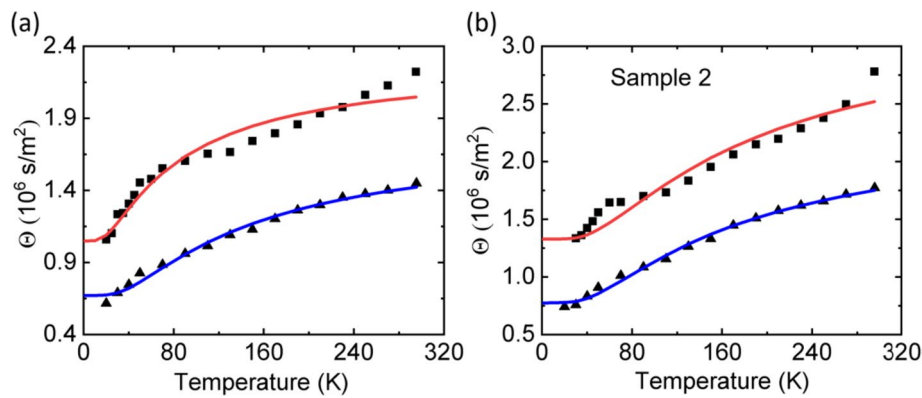


Fig. 11 Θ - T of two reduced graphene oxide microfibers before and after thermal annealing, respectively [79]. The parallel trend of Θ - T curves can be observed for both samples. Θ_0 is fitted based on the thermal reffusivity model in Eq. (7), where a significant reduction of Θ_0 demonstrates the structural domain size is greatly increased by thermal annealing treatment. (Reprinted from Carbon, 203, Lin et al., Ultra-high thermal sensitivity of graphene microfiber, 620–629, Copyright 2023, with permission from Elsevier.)

the thermal reffusivity is defined as: $\Theta = C_e/k$. Here C_e is the specific heat of free electrons ($C_e = \gamma T$ with γ as a constant), and metal's thermal conductivity k is mainly sustained by free electrons [73]. For phonons, the thermal reffusivity is defined as: $\Theta = 1/\alpha$, where α is thermal diffusivity [72]. If the phonon velocity of a material is independent of temperature (which is a good approximation for most of materials), Θ of phonons can be expressed as a function of temperature as [71, 72]:

$$\Theta = \Theta_0 + C_\Theta \times e^{-\theta/2T}. \quad (7)$$

Here C_Θ is a constant. Θ_0 is the “residual thermal reffusivity” at the 0 K limit, which is solely resulted from structural defects induced phonon scattering. It can be further expressed in terms of the phonon mean free path induced solely by structure (l_0) as: $\Theta_0 = 3/(vl_0)$ (for isotropic material). l_0 is an effective structure thermal domain (STD) size accounting for all structural defect effects on phonon-scattering, whose value is comparable to the crystallite size characterized by x-ray diffraction. The second part on the right of the equation is associated with Umklapp phonon scattering, whose intensity is determined by the phonon population participating in heat conduction. For normal materials, Umklapp phonon scattering dominates heat conduction at high temperatures. The slope of Θ - T curves is determined by the Debye temperature. As temperature goes down, Θ decreases and approaches to a residual value Θ_0 , which is determined by the defect density and structural domain size of the test-material. For highly defected materials or materials with strong interface effect, however, Θ could stay almost constant in the whole temperature range, demonstrating the dominating role of structural defects/interfaces induced phonon scattering in thermal conduction [74, 75].

Based on the experimentally measured Θ - T curves, the thermal reffusivity model is advantageous in analyzing the Debye temperature, structural defect levels, and the structural thermal domain sizes in various materials [72, 73, 76, 77]. Even for single-walled carbon nanotubes with nanoscale scattering cross section, the average structure thermal domain size could be measured based on the thermal reffusivity model [78]. To show the application of thermal reffusivity model, Fig. 11 shows the experimentally measured Θ - T curves of two reduced graphene oxide microfibers before and after thermal annealing, respectively [79]. The significantly reduced Θ_0 value at the 0 K limit showed that the defect-induced phonon mean free path increases greatly after thermal annealing, indicating a much larger STD size. It is also interesting to observe the parallel feature of the Θ - T curves before and after thermal annealing. The similar slope of the Θ - T curves demonstrate that the inner connecting strength (reflected in the Debye temperature) is not significantly changed by thermal annealing. Compared with the traditionally used thermal conductivity (κ) against temperature curves, the Θ - T curves provide a much clearer observation and more effective analysis for understanding the structural effect on thermal transport. For most cases, the κ - T curves contains complex information about the temperature dependency of specific heat, which overshadows the phonon scattering effect; while the Θ - T model directly characterizes the phonon scattering intensity.

B. Effective interface energy transmission velocity

Understanding phonon transport across material interfaces is crucial, especially in heterogeneous materials. The study of this phenomenon under the continuum theory is primarily guided by two theoretical models: the

Acoustic Mismatch Model (AMM) and the Diffuse Mismatch Model (DMM). These models provide frameworks for predicting and analyzing the behavior of phonons at the interface. The AMM, based on the acoustic theory of wave propagation, is effective in scenarios involving atomically smooth and well-ordered interfaces. This model utilizes the concept of acoustic impedance, a factor dependent on the material's density (ρ) and sound velocity (v). In AMM, phonons are considered analogous to acoustic waves, with their transmission and reflection at an interface determined by the acoustic impedance mismatch between the adjoining materials. A higher mismatch results in increased phonon reflection, and a lower mismatch favors transmission. The AMM has been instrumental in calculating the interfacial thermal conductance (G), particularly in semiconductors and insulators. However, its applicability is limited in cases with significant structural disorder at the interfaces.

Conversely, the DMM addresses interfacial phonon transport in materials with rough or imperfect interfaces. It diverges from the specular phonon transport assumption of the AMM and considers that phonons are diffusely scattered at the interface, leading to a loss of phonon directional memory. The DMM is thus more relevant for interfaces in polycrystalline materials, thin films, or materials with lattice disorder, offering a comprehensive approach to modeling thermal conductance in these contexts. Both models have their respective strengths and limitations. The AMM provides accurate predictions for clean and well-ordered interfaces, while the DMM is better suited for interfaces characterized by roughness or disorder. Both models have their respective strengths and limitations. In terms of practical applications for thermal managements, the design often focuses on minimizing acoustic impedance mismatch to enhance thermal transport across interfaces, which is essential in microelectronics for efficient heat dissipation and maintaining optimal junction temperatures. The determination of G is a critical aspect of these models. G is primarily influenced by the transmissivity of phonons at interfaces, with the phonon mean free path within each solid being a significant factor. The consideration of G is particularly relevant in ultra-thin films where traditional temperature definitions based on thermal equilibrium are not applicable. Here, temperature is interpreted as an average energy representation of phonons, aligning with the equilibrium temperature that phonons would have upon redistributing adiabatically.

In the diffuse mismatch model, the calculation of G can be simplified as: $G = \left[(\pi/15)(k_B^4/\hbar^3) \sum_j v_{i,j}^{-2} \bar{\alpha}_i(\omega) \right] T^3$ where k_B is the Boltzmann constant, \hbar is the reduced Planck constant, and $\bar{\alpha}_i(\omega)$ the averaged transmission probability

of phonons. Here, i denotes the side of the interface and goes from 1 to 2, j denotes the phonon mode, which are restricted to the acoustic modes at each side, and v is the phonon group velocity. The T^3 dependency in the G relation is analogous to the dependency of the specific heat in the Debye model. It is worth noting that the transmission coefficient $\alpha_i(\omega)$ is effectively calculated by the mismatch in the density of states for the two materials across the interface. The Debye approximation of linear dispersion allows to calculate the average transmission coefficient as:

$$\bar{\alpha}_i(\omega) = \left(\frac{1}{2} \right) \sum_j v_{3-i,j}^{-2} / \sum_{i,j} v_{i,j}^{-2}.$$

Classically, G under the diffuse limit can be further approximated as $G = (T_{d12} C_1 v_1)/4$ [80], where T_{d12} is the phonon transmissivity at the interface and can be calculated as $T_{dij} = C_j v_j / (C_i v_i + C_j v_j)$ [81], C is the volumetric heat capacity and v the phonon group velocity, which can be obtained under the Debye approximation or from the dispersion relations [82] for more accurate calculations.

In ultra-thin films, traditional equilibrium thermodynamics is insufficient due to non-equilibrium conditions. Here, temperature is redefined as the average phonon energy at a given point, anticipating an equilibrium temperature achievable through adiabatic redistribution. This redefinition deviates from the classical G concept, which relies on emitted phonon temperatures where equivalent equilibrium temperatures at the interface do not align with the temperatures of emitted phonons. The framework proposed by Simon [83], which utilizes equivalent equilibrium temperatures of phonons on both sides of an interface, offers a more accurate representation for G in such nonequilibrium systems. Under these assumptions, G can be expressed using the following equation: $G = (T_{d21} C_2 v_2) / (4[1 - 0.5(T_{d12} + T_{d21})])$. Several modifications have been attempted in literatures to improve the accuracy of DMM calculations. Beechem et al. [82] further improved upon this by including the effects of optical phonon modes noting the significant role of these modes despite their lower group velocities. Hopkins and Norris [84] introduced an alternative approach by using joint vibrational states defined by phonons on both sides of the interface, essentially replacing the phonons at the interface itself. Loh et al. [85] then extended the DMM to account for the influence of thermal flux on phonon transmission. Furthermore, the DMM was expanded by incorporating inelastic scattering effects [86] and the impact of disorder on G [87].

Inspired by the previous continuum models, and to subtract the impact of heat capacity on the energy transport variation across the interface, we introduce a concept termed effective interface energy transmission velocity (termed " $v_{i,eff}$ " hereafter), which is defined as $v_{i,eff} = G/\rho c_p$. We expect this parameter to give an

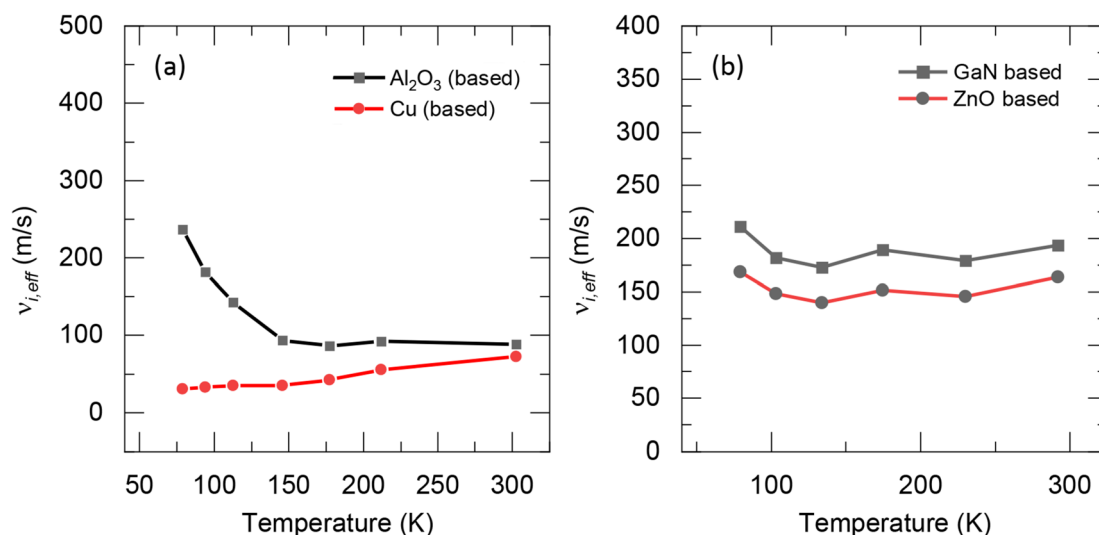


Fig. 12 The variation of the effective interface energy transmission velocity with temperature for (a) Cu/Al₂O₃ [88] and (b) ZnO/GaN [89] interfaces

intrinsic picture of the transmission of heat carriers, unaltered by the influence of their capacity to carry the heat. We process several interfaces for which G is reported in literatures to analyze how $v_{i,eff}$ varies with temperature. Very strikingly, we observe an almost constant value over a wide range of temperatures, particularly at high temperatures. For instance, Fig. 12a shows the variation of $v_{i,eff}$ for Cu/Al₂O₃ interface [88]. Since $v_{i,eff}$ involves accounting for the specific heat, we process the data twice based on the specific heat of each material. We observe that the $v_{i,eff}$ values are roughly around 100 m/s especially for temperatures above 150 K. The discrepancies in the trend between the two curves can be explained by the large mismatch in the Debye temperature of each side (347 and 980 K for Cu and Al₂O₃, respectively), which dictates the behavior of the specific heat with temperatures. At low temperatures, the impact of mismatch in the Debye temperature is more prominent where it yields an obvious variation for $v_{i,eff}$.

On the other hand, Fig. 12b which examines the ZnO/GaN interface [89] shows almost similar trend, unlike the Cu/Al₂O₃ interface. This also can be explained by the relatively matching Debye temperatures (650 and 416 K for GaN and ZnO, respectively). The velocity seems to be constant around 170–190 m/s. We find the range of $v_{i,eff}$ to be consistent with the classical results $v_{i,eff} \sim T_{d12}v_1/4$. For instance, GaN has a $v_{LA} \sim 6.9$ and $v_{TA} \sim 5.0$ km/s. The average phonon group velocity can be calculated as $3/v_{avg} = 1/v_{LA} + 2/v_{TA}$ which yields a value of ~ 5.5 km/s. Using the previous formula, we estimate the average transmission coefficient to be $\sim 14.5\%$. We note that the above discussion is limited to dealing with phonons of each side of the interface independently and does not incorporate the impact of their interactions

which will ultimately dictate how $v_{i,eff}$ changes with temperature. For energy transport across an interface sustained by phonons, the underlying physics in fact is the interaction between atom-pair across the interface. This cross-interface inter-atomic action in fact prompts a third type of phonons, coined "interface phonons", that are different from those of both sides of the interface. Therefore, the specific heat to be used in $v_{i,eff}$ calculation should that of interface phonons. For phonons sustained by covalent bonds, its volumetric specific heat varies, but is pretty much in the same order at any specified temperature. For instance, at room temperature, ρc_p of most solids falls in the range of $1.5 \sim 2.5 \times 10^6$ J/m³. Therefore, for the interfaces discussed above, even when the specific heat of interface phonons are used, $v_{i,eff}$ will not differ significantly. Further model development for this theory is still going on in our lab and will be published in the near future.

5 Concluding remarks and outlook

To understand the interfacial thermal transport from experiments, various techniques have been developed including the 3ω technique, PTR technique, TDTR, FDTR, and SS-Raman techniques. In this perspective, we systematically reviewed the transient opto-thermal Raman-based techniques developed in recent years for measuring the interfacial thermal resistance between 2D materials and substrate. These transient Raman techniques show great advantages for not only being noncontact and nondestructive, but also avoids the uncertainties from laser absorption coefficient and absolute temperature rise. The energy transport among carriers in a 2D material during and after laser irradiation is

first introduced for furthering understanding of the transient process. The TD-Raman and FR-Raman involve probing a material's thermal response in time and frequency domains. The TD-Raman features a high sensitivity over FR-Raman, but has very weak Raman signal when the heating time is very short. In addition, the laser flash Raman is another powerful technique for detecting the transient thermal response. To push the temporal resolution of Raman spectroscopy to hundreds of picoseconds, dual-wavelength laser flash Raman spectroscopy was further developed.

Out of the Raman techniques for interface thermal transport characterization, the ET-Raman probably provides the best solution. It features very high sensitivity, being able to reach ps resolution, and could distinguish the phonon and hot carrier transport. The hot carrier diffusion effect is a critical process and must be considered when the laser spot size is small, e.g. 0.2~0.3 μm radius. The thermal nonequilibrium among phonon branches for both suspended and supported 2D materials is very challenging to quantify. The thermal field invariant technique is the best one for distinguishing OP and AP temperatures for suspended 2D materials. For supported 2D materials in interface characterization, it remains a great challenge to distinguish OP and AP temperatures.

Compared with the thermal conductivity-temperature curves, the thermal reffusivity model provides a much clearer observation and more effective analysis for understanding the structural effect on thermal transport in solids. To understand phonon transport across material interfaces, the AMM and DMM still have much room for improvement in physics understanding. Inspired by the thermal reffusivity theory, a new concept termed "effective interface energy transmission velocity" ($v_{i,eff}$) is introduced. It provides significant physical meaning in understanding the interface energy transport mechanism. We observed an almost constant $v_{i,eff}$ value over a wide temperature range for many reported interfaces. This new model is very promising to give an intrinsic picture of the transmission of heat carriers, unaltered by the influence of their capacity to carry heat.

Acknowledgements

This work was supported by the National Natural Science Foundation of China (No.12204320 for J.L. and 52276080 for Y.X.) and US National Science Foundation (CBET1930866 and CMMI2032464 for X.W). J.L. is grateful for the support from Shenzhen Science and Technology Program (JCYJ20220530153401003).

Author contributions

X.Wang conceived the review idea. All authors participated in manuscript preparation. Y. Xie and X. Wang conducted draft revision.

Availability of data and materials

Data is available upon reasonable request from readers.

Declarations

Competing interests

The authors declare no competing interests.

Received: 29 December 2023 Revised: 21 January 2024 Accepted: 22 January 2024

Published online: 08 February 2024

References

- Gu XK et al (2018) Colloquium: phononic thermal properties of two-dimensional materials. *Rev Mod Phys* 90(4):041002
- Xiang R (2022) Atomic precision manufacturing of carbonnanotube-a perspective. *Int J Extrem Manuf* 4:023001
- Seol JH et al (2010) Two-dimensional phonon transport in supported graphene. *Science* 328(5975):213–216
- Das S et al (2021) Transistors based on two-dimensional materials for future integrated circuits. *Nat Electron* 4(11):786–799
- Yalon E et al (2017) Energy dissipation in monolayer MoS_2 electronics. *Nano Lett* 17(6):3429–3433
- Yue YN et al (2017) Energy coupling across low-dimensional contact interfaces at the atomic scale. *Int J Heat Mass Transf* 110:827–844
- Chen Z et al (2009) Thermal contact resistance between graphene and silicon dioxide. *Appl Phys Lett* 95(16):161910
- Wang XW, Zhong ZR, Xu J (2005) Noncontact thermal characterization of multiwall carbon nanotubes. *J Appl Phys* 97(6):064302
- Chen XW et al (2010) Thermophysical properties of hydrogenated vanadium-doped magnesium porous nanostructures. *Nanotechnology* 21(5):055707
- Villaroman D et al (2017) Interfacial thermal resistance across graphene/ Al_2O_3 and graphene/metal interfaces and post-annealing effects. *Carbon* 123:18–25
- Capinski WS et al (1999) Thermal-conductivity measurements of GaAs/AlAs superlattices using a picosecond optical pump-and-probe technique. *Phys Rev B* 59(12):8105–8113
- Eesley GL (1983) Observation of nonequilibrium electron heating in copper. *Phys Rev Lett* 51:2140–2143
- Cahill DG (2004) Analysis of heat flow in layered structures for time-domain thermoreflectance. *Rev Sci Instrum* 75(12):5119–5122
- Jiang PQ et al (2017) Probing anisotropic thermal conductivity of transition metal dichalcogenides MX_2 ($\text{M} = \text{Mo}, \text{W}$ and $\text{X} = \text{S}, \text{Se}$) using time-domain thermoreflectance. *Adv Mater* 29(36):1701068
- Schmidt AJ, Chen XY, Chen G (2008) Pulse accumulation, radial heat conduction, and anisotropic thermal conductivity in pump-probe transient thermoreflectance. *Rev Sci Instrum* 79(11):114902
- Qian X et al (2020) Accurate measurement of in-plane thermal conductivity of layered materials without metal film transducer using frequency domain thermoreflectance. *Rev Sci Instrum* 91(6):064903
- Freedman JP et al (2013) Universal phonon mean free path spectra in crystalline semiconductors at high temperature. *Sci Rep* 3:2963
- Zhu J et al (2010) Ultrafast thermoreflectance techniques for measuring thermal conductivity and interface thermal conductance of thin films. *J Appl Phys* 108(9):094315
- Balandin AA et al (2008) Superior thermal conductivity of single-layer graphene. *Nano Lett* 8(3):902–907
- Chen SS et al (2011) Raman measurements of thermal transport in suspended monolayer graphene of variable sizes in vacuum and gaseous environments. *ACS Nano* 5(1):321–328
- Yan RS et al (2014) Thermal conductivity of monolayer molybdenum disulfide obtained from temperature-dependent Raman spectroscopy. *ACS Nano* 8(1):986–993
- Yu YF et al (2020) In-plane and interfacial thermal conduction of two-dimensional transition-metal dichalcogenides. *Phys Rev Appl* 13(3):034059
- Cai WW et al (2010) Thermal transport in suspended and supported monolayer graphene grown by chemical vapor deposition. *Nano Lett* 10(5):1645–1651

24. Liu J et al (2022) Photothermal phenomenon: extended ideas for thermo-physical properties characterization. *J Appl Phys* 131(6):065107
25. Cheng Z et al (2019) Thermal conductance across β -GaO-diamond van der Waals heterogeneous interfaces. *APL Mater* 7(3):031118
26. Cheng Z et al (2020) Interfacial thermal conductance across room-temperature-bonded GaN/Diamond interfaces for GaN-on-diamond devices. *ACS Appl Mater Interfaces* 12(7):8376–8384
27. Bao W et al (2023) Thermal transport across graphene/GaN and MoS₂/GaN interfaces. *Int J Heat Mass Transf* 201:123569
28. Wu X, Tang W, Xu X (2020) Recent progresses of thermal conduction in two-dimensional materials. *Acta Phys Sin* 69:37–69
29. Hopkins PE et al (2012) Manipulating thermal conductance at metal-graphene contacts via chemical functionalization. *Nano Lett* 12(2):590–595
30. Kim J et al (2016) Bimodal control of heat transport at graphene-metal interfaces using disorder in graphene. *Sci Rep* 6:34428
31. Zobeiri H et al (2022) Robust and high-sensitivity thermal probing at the nanoscale based on resonance Raman ratio (R₃). *Int J Extreme Manuf* 4(3):035201
32. Wang RD et al (2020) Thermal behavior of materials in laser-assisted extreme manufacturing: Raman-based novel characterization. *Int J Extreme Manuf* 2(3):032004
33. Wang RD et al (2022) Critical problems faced in Raman-based energy transport characterization of nanomaterials. *Phys Chem Chem Phys* 24(37):22390–22404
34. Xu S et al (2020) Raman-based nanoscale thermal transport characterization: a critical review. *Int J Heat Mass Transf* 154:119751
35. Zobeiri H et al (2019) Frequency-domain energy transport state-resolved Raman for measuring the thermal conductivity of suspended nm-thick MoSe. *Int J Heat Mass Transf* 133:1074–1085
36. Wang TY et al (2016) Frequency-resolved Raman for transient thermal probing and thermal diffusivity measurement. *Opt Lett* 41(1):80–83
37. Xu S et al (2015) Development of time-domain differential Raman for transient thermal probing of materials. *Opt Express* 23(8):10040–10056
38. Hunter N et al (2022) Interface thermal resistance between monolayer WSe₂ and SiO₂: Raman probing with consideration of optical-acoustic phonon nonequilibrium. *Adv Mater Interfaces* 9(7):2102159
39. Yuan PY et al (2018) Nonmonotonic thickness-dependence of in-plane thermal conductivity of few-layered MoS₂: 2.4 to 37.8 nm. *Phys Chem Chem Phys* 20(40):25752–25761
40. Yuan PY et al (2017) The hot carrier diffusion coefficient of sub-10 nm virgin MoS₂: uncovered by non-contact optical probing. *Nanoscale* 9(20):6808–6820
41. Liu JH et al (2019) Differential laser flash Raman spectroscopy method for non-contact characterization of thermal transport properties of individual nanowires. *Int J Heat Mass Transf* 135:511–516
42. Fan AR et al (2019) Laser flash Raman spectroscopy method for characterizing the specific heat of a single nanoparticle. *J Nanosci Nanotechnol* 19(11):7004–7013
43. Fan AR et al (2019) Dual-wavelength flash Raman mapping method for measuring thermal diffusivity of suspended 2D nanomaterials. *Int J Heat Mass Transf* 143:118460
44. Fan A et al (2021) Two-step dual-wavelength flash raman mapping method for measuring thermophysical properties of supported 2D nanomaterials. *Heat Transf Eng* 43:1627–1638
45. Yuan PY et al (2017) Energy transport state resolved Raman for probing interface energy transport and hot carrier diffusion in few-layered MoS. *ACS Photonics* 4(12):3115–3129
46. Yuan PY et al (2018) Very fast hot carrier diffusion in unconstrained MoS₂ on a glass substrate: discovered by picosecond ET-Raman. *RSC Adv* 8(23):12767–12778
47. Vallabhaneni AK et al (2016) Reliability of Raman measurements of thermal conductivity of single-layer graphene due to selective electron-phonon coupling: a first-principles study. *Phys Rev B* 93(12):125432
48. Lee H et al (2016) Graphene-semiconductor catalytic nanodiodes for quantitative detection of hot electrons induced by a chemical reaction. *Nano Lett* 16:1650–1656
49. Trovattello C et al (2022) Ultrafast hot carrier transfer in WS₂/graphene large area heterostructures. *NPJ 2D Mater Appl* 25(6): 1–8
50. Lee YK et al (2016) Hot carrier multiplication on graphene/TiO₂ Schottky nanodiodes. *Sci Rep* 6:27549
51. Massicotte M et al (2021) Hot carriers in graphene-fundamentals and applications. *Nanoscale* 13:8376–8411
52. Lu ZX et al (2018) Phonon branch-resolved electron-phonon coupling and the multitemperature model. *Phys Rev B* 98(13):134309
53. Wang TY et al (2018) Characterization of anisotropic thermal conductivity of suspended nm-thick black phosphorus with frequency-resolved Raman spectroscopy. *J Appl Phys* 123(14):145104
54. Wang R, Zobeiri H, Xie Y, Wang X, Zhang X, Yue Y (2020) Distinguishing optical and acoustic phonon temperatures and their energy coupling factor under photon excitation in nm 2D materials. *Adv Sci* 7:2000097
55. Zobeiri H et al (2021) Interfacial thermal resistance between nm-thick MoS₂ and quartz substrate: a critical revisit under phonon mode-wide thermal non-equilibrium. *Nano Energy* 89:106364
56. Zobeiri H et al (2021) Direct characterization of thermal nonequilibrium between optical and acoustic phonons in graphene paper under photon excitation. *Adv Sci* 8(12):2004712
57. Xu S et al (2022) Distinct optical and acoustic phonon temperatures in nm-thick suspended WS₂: direct differentiating via acoustic phonon thermal field invariant. *Materials Today Physics* 27:100816
58. Li QY, Zhang X, Hu YD (2014) Laser flash Raman spectroscopy method for thermophysical characterization of 2D nanomaterials. *Thermochim Acta* 592:67–72
59. Li QY, Ma WG, Zhang X (2016) Laser flash Raman spectroscopy method for characterizing thermal diffusivity of supported 2D nanomaterials. *Int J Heat Mass Transf* 95:956–963
60. Li QY et al (2017) Measurement of specific heat and thermal conductivity of supported and suspended graphene by a comprehensive Raman optothermal method. *Nanoscale* 9(30):10784–10793
61. Li QY, Zhang X, Takahashi K (2018) Variable-spot-size laser-flash Raman method to measure in-plane and interfacial thermal properties of 2D van der Waals heterostructures. *Int J Heat Mass Transf* 125:1230–1239
62. Hunter N et al (2020) Interfacial thermal conductance between monolayer WSe₂ and SiO₂ under consideration of radiative electron-hole recombination. *ACS Appl Mater Interfaces* 12(45):51069–51081
63. Zobeiri HW, Wang R et al (2019) Hot carrier transfer and phonon transport in suspended nm WS₂ films. *Acta Mater* 175:222–237
64. Lu Z, Ruan X (2019) Non-equilibrium thermal transport: a review of applications and simulation approaches. *ES Energy Environ* 4:5–14
65. Patterson DJ, Bailey CB (2011) Solid-state physics: introduction to the theory 2nd edn. Springer, Cham, Switzerland
66. Lindsay L, Broilo DA, Mingo N (2011) Flexural phonons and thermal transport in multilayer graphene and graphite. *Phys Rev B* 83(23):235428
67. Guo YY et al (2023) Basal-plane heat transport in graphite thin films. *Phys Rev B* 107(19):195430
68. Yu CQ et al (2023) Characteristics of distinct thermal transport behaviors in single-layer and multilayer graphene. *Phys Rev B* 107(16):165424
69. Feng TL, Lindsay L, Ruan XL (2017) Four-phonon scattering significantly reduces intrinsic thermal conductivity of solids. *Phys Rev B* 96(16):161201
70. Tang JL et al (2023) Effect of four-phonon scattering on anisotropic thermal transport in bulk hexagonal boron nitride by machine learning interatomic potential. *Int J Heat Mass Transf* 207:124011
71. Xie YS et al (2018) Thermal reffusivity: uncovering phonon behavior, structural defects, and domain size. *Front Energy* 12(1):143–157
72. Xie YS et al (2015) The defect level and ideal thermal conductivity of graphene uncovered by residual thermal reffusivity at the 0 K limit. *Nanoscale* 7(22):10101–10110
73. Cheng Z et al (2015) Temperature dependence of electrical and thermal conduction in single silver nanowire. *Sci Rep* 5:10718
74. Xie YS et al (2016) Interface-mediated extremely low thermal conductivity of graphene aerogel. *Carbon* 98:381–390
75. Liu J et al (2017) Thermal conductivity and annealing effect on structure of lignin-based microscale carbon fibers. *Carbon* 121:35–47
76. Liu J et al (2015) thermal conductivity of ultrahigh molecular weight polyethylene crystal: defect effect uncovered by 0 K limit phonon diffusion. *ACS Appl Mater Interfaces* 7(49):27279–27288
77. Zhu BW et al (2017) novel polyethylene fibers of very high thermal conductivity enabled by amorphous restructuring. *ACS Omega* 2(7):3931–3944
78. Rahbar M et al (2023) Observing grain boundary-induced phonons mean free path in highly aligned SWCNT bundles by low-momentum phonon scattering. *Cell Rep Phys Sci* 4:101688

79. Lin H et al (2023) Ultra-high thermal sensitivity of graphene microfiber. *Carbon* 203:620–629
80. Chen G (1998) Thermal conductivity and ballistic-phonon transport in the cross-plane direction of superlattices. *Phys Rev B* 57(23):14958
81. Swartz ET, Pohl RO (1989) Thermal boundary resistance. *Rev Mod Phys* 61(3):605–668
82. Beechem T et al (2010) Contribution of optical phonons to thermal boundary conductance. *Appl Phys Lett* 97(6):061907
83. Simons S (1974) On the thermal contact resistance between insulators. *J Phys C: Solid State Phys* 7(22):4048
84. Hopkins PE, Norris PM (2007) Effects of Joint Vibrational States on Thermal Boundary Conductance. *Nanoscale Microscale Thermophys Eng* 11(3–4):247–257
85. Loh GC, Tay BK, Teo EHT (2010) Flux-mediated diffuse mismatch model. *Appl Phys Lett* 97(12):121917
86. Duda JC et al (2010) Inelastic phonon interactions at solid-graphite interfaces. *Superlattices Microstruct* 47(4):550–555
87. Beechem T, Hopkins PE (2009) Predictions of thermal boundary conductance for systems of disordered solids and interfaces. *J Appl Phys* 106(12):124301
88. Gundrum BC, Cahil DGI, Averback RS (2005) Thermal conductance of metal-metal interfaces. *Phys Rev B* 72(24):245426
89. Gaskins JT et al (2018) Thermal boundary conductance across heteroepitaxial ZnO/GaN interfaces: assessment of the phonon gas model. *Nano Lett* 18(12):7469–7477

Publisher's Note

Springer Nature remains neutral with regard to jurisdictional claims in published maps and institutional affiliations.